Wave Front Sensing demodulated at the difference frequency between two phase-modulation sidebands in a compound interferometer configuration for a gravitational-wave detector

Chiaki Hirose¹, Kenta Tanaka², Osamu Miyakawa², and Takafumi Ushiba²

¹Graduate School of Science and Technology, Niigata University, Nishi-ku, Niigata City, Niigata 950-2181, Japan

 $^*E\text{-}mail: f22l003c@mail.cc.niigata\text{-}u.ac.jp$

²Institute for Cosmic Ray Research (ICRR), KAGRA Observatory, The University of Tokyo, Kamioka-cho, Hida City, Gifu 506-1205, Japan

> Precise alignment sensing and control are essential for maintaining the stability of laser interferometric gravitational-wave detectors. Conventional Wave Front Sensing technique (WFS), which relies on the beat between the carrier and phase-modulated (PM) sidebands, is dominated by arm-axis signals when the carrier resonates in the full interferometer. This dominance limits the detection of other optical axes, such as the Power Recycling Cavity (PRC) and incident beam axes. To address this problem, we propose a novel sensing technique, "Phase-Modulated-sideband × Phase-Modulated-sideband Wave Front Sensing" (PMPMWFS), which demodulates the beat signal at the difference frequency between two anti-resonant PM sidebands. We derived the theoretical response of PMPMWFS and experimentally demonstrated it using the Power-Recycled X-arm (PRXARM) configuration of KAGRA. The results show that PMPMWFS effectively decouples angular fluctuation signals of the PRC and incident beam from those of the arm cavity and provides orthogonal signal components for the end mirror of the arm cavity. Furthermore, feedback control using PMPMWFS achieved stable interferometer locking for over one hour. These results demonstrate that PMPMWFS offers an effective sensing method for decoupling multiple alignment degrees of freedom in future gravitational-wave detectors.

......

Subject Index xxxx, xxx

1 Introduction.

Gravitational Waves (GWs) are ripples in spacetime that propagate at the speed of light, generated by the accelerated motion of massive objects [1]. Observable GWs are emitted by astrophysical phenomena such as the mergers of compact binaries, the rotational motion of pulsars, and supernova explosions. The direct detection of these GWs is expected to yield significant scientific outcomes, including measurements of the Hubble constant [2] and the verification of general relativity [3]. This is achieved using laser interferometric GW detectors, each of which combines multiple optical resonators.

Determining the direction of the GW source using laser interferometric GW detectors requires the detection of the time difference in the arrival of the GW at multiple detectors. As an example, on 14 August 2017, simultaneous GW observations were achieved for the first time by Advanced LIGO [4] and Advanced Virgo [5], with greater precision than in previous observations [6]. Therefore, it is important to operate GW detectors stably over the long term.

In laser interferometric GW detectors that incorporate multiple optical cavities, angular fluctuations of the mirrors constituting the interferometer can cause a relative misalignment between the incident beam axis and the resonant cavity axes, potentially reducing the stability of the interferometer. The interferometer stability can be improved by detecting this relative misalignment and feeding back to the mirror angles.

Wave Front Sensing technique (WFS) is primarily employed to detect optical axis misalignment in interferometers [7]. The laser beam incident on the interferometer with multiple optical resonators is phase-modulated to generate sidebands using an Electro Optic Modulator (EOM). The beam reflected from the resonator is detected by a Quadrant Photo Diode (QPD). By demodulating the detection signal at the phase modulation frequency, the relative misalignment between the optical axis of the phase-modulated sideband (PM sideband) and that of the carrier is measured.

Japanese GW detector KAGRA [8] conducted joint observations with LIGO during the fourth international collaborative GW observation run (O4a) [9], from 24 May to 20 June 2023 (UTC). KAGRA employed a Power Recycled Fabry-Pérot Michelson Interferometer (PRFPMI) during O4a. The PRFPMI consists of a Fabry-Pérot Cavity (FPC) in each arm of the Michelson Interferometer (MI) called X- and Y- arm cavity, and the Power Recycling Mirror (PRM) recycles the light reflected from the interferometer. The Power Recycling Cavity (PRC) increases the intracavity power in the FPCs at both arms, reducing the shot noise that limits the sensitivity. The primary degrees of freedom of the optical axis in the PRFPMI are the FPC axes of both arms, the MI axis, the PRC axis, and the incident light

axis. To reduce thermal noise, KAGRA adopts a large beam size on the FPC mirrors, making the optical axis more prone to tilting than in the other cavities. This FPC configuration is not unique to KAGRA but is also common to other large-scale laser interferometric GW detectors, such as LIGO and Virgo.

When the carrier component resonates in the entire interferometer including the arm cavities, the WFS signal using the carrier detects changes in all axes. Consequently, the signal from the arm cavity makes it difficult to discern the signals from other axes in the WFS signal, because the arm cavity axis is the most sensitive to the angular motion of mirrors. As a result, it becomes difficult to stabilize the interferometer by feedback control. In the future, KAGRA will be upgraded to the Resonant Sideband Extraction (RSE) [10] to broaden the detection bandwidth for GW signals. Due to the increased number of degrees of freedom requiring control, this issue will become more pronounced, making signal separation crucial.

In this paper, we propose a new alignment detection scheme, "Phase-Modulated-sideband × Phase-Modulated-sideband Wave Front Sensing" (PMPMWFS), which uses the difference frequency of two PM sidebands. This method is designed to detect the optical axis difference between the cavity axis and the incident axis to the cavity by tuning PM sideband frequencies so that one of them resonates on the cavity and the other does not. Specifically, the two sidebands adopted here (Fig. 1) do not resonate in the arm cavities. Therefore, the ratio of the arm cavity axis fluctuation signal to the signals from other optical axes detected by the PMPMWFS is expected to be smaller than that in the WFS signal. If the PMPMWFS can achieve signal separation between the fluctuations of the incident beam and the PRC axis from those of the arm cavity, it will provide an effective means of alignment control to stabilize the interferometer.

This paper summarizes the derivation of the PMPMWFS signal in Sec. 2. In Section 3, we present the results of measuring the PMPMWFS signal in the PRXARM, in which KAGRA's PRC and X-arm cavity are resonant, and demonstrate alignment control of KAGRA's interferometer using the PMPMWFS signal.

2 Derivation of the PMPMWFS.

This section presents the theoretical derivation of the PMPMWFS signal for a composite optical resonator. Section 2.1 describes the interferometer configuration of the composite optical resonator used in the theoretical analysis of the PMPMWFS signal. Section 2.2 shows the electric field of the reflected light from the composite optical resonator for the fundamental Gaussian mode and the first-order Hermite-Gaussian mode. Section 2.3 details

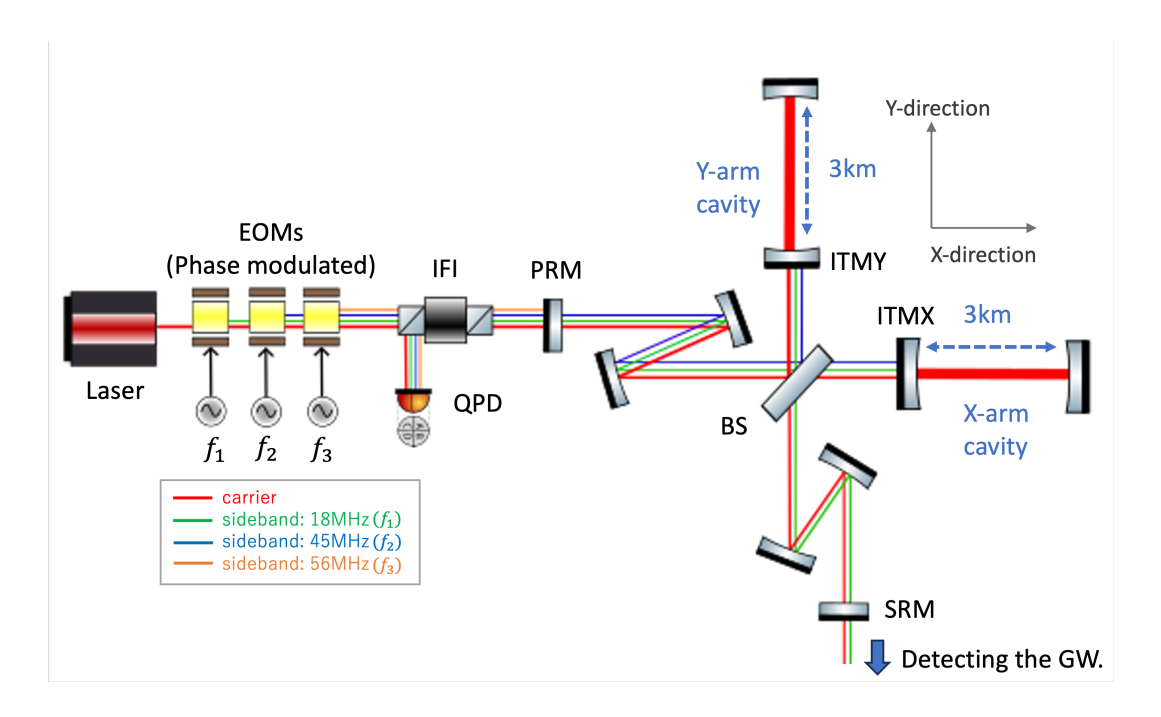


Fig. 1: RSE schematic diagram in KAGRA. The incident light is split by a BS into the X- and Y-directions. FPCs are installed in both arms of the MI, referred to as the X- and Y-arm cavity. A PRM forms a PRC with the two input mirrors of the FPCs (ITMX and ITMY). Similarly, a Signal Recycling Mirror (SRM) forms a Signal Recycling Cavity (SRC) with the ITMs. The gravitational wave signal is detected at the SRC's output port as a change in the optical path difference between the two arm cavities. Three PM sidebands are generated by the EOMs. The carrier beam resonates in both the PRC and the arm cavities. The PM sidebands f_1 , f_2 , and f_3 exhibit distinct resonance states: f_1 resonates with both the PRC and SRC, f_2 resonates only with the PRC, and f_3 is anti-resonant with all resonators. The reflected light from the interferometer is redirected by an Input Faraday Isolator (IFI) and detected by the QPDs.

the derivation of the PMPMWFS signal obtained from the reflected light of the composite optical resonator.

2.1 Model for the PMPMWFS derivation.

Two EOMs are placed in series immediately after the laser source. The laser beam is phase-modulated by the EOMs to generate two PM sidebands f_a and f_b ($f_a > f_b$), and is then injected into the composite optical resonator. The light reflected from the composite optical resonator is detected by a QPD. The QPD signal is demodulated at the difference

frequency $(f_a - f_b)$ between the two PM sideband frequencies. After the demodulated signal passes through a low-pass filter, the PMPMWFS signal is obtained.

When the angles of the mirrors constituting the composite optical resonator fluctuate, the reflectance of the first-order Gaussian beam components change for the carrier and the two PM sidebands. Therefore, by describing the PMPMWFS signal in terms of these reflectance, we derive how the mirror misalignment is manifested in the PMPMWFS signal.

2.2 Derivation of the electric field reflected from the composite optical cavity.

The time variation of the output electric field from the laser can be expressed as follows:

$$E_1 = E_0 e^{i\Omega t},\tag{1}$$

where E_0 and Ω are the amplitude and angular frequency of the laser, respectively.

The electric field E_{inc} , when the sidebands f_{a} and f_{b} are phase-modulated in series, can be expressed as follows:

$$E_{\rm inc} = E_1 e^{i(m_a \cos \omega_a t + m_b \cos \omega_b t)}, \tag{2}$$

where the modulation angular frequencies are denoted by $\omega_{\rm a}$ and $\omega_{\rm b}$, and the modulation indices are denoted by $m_{\rm a}$ and $m_{\rm b}$.

Expanding Eq. 2 into a series using the Bessel function $J_n(m_a)$ and $J_n(m_b)$ gives the following expression:

$$E_{\rm inc} = E_1(\sum_{n=-\infty}^{\infty} J_n(m_{\rm a})(i)^n e^{in\omega_{\rm a}t}) \left(\sum_{n=-\infty}^{\infty} J_n(m_{\rm b})(i)^n e^{in\omega_{\rm b}t}\right). \tag{3}$$

Assuming both modulation indices satisfy $m_a, m_b \ll 1$, the higher-order terms of the Bessel function are negligible. Therefore, $E_{\rm inc}$ can be approximated by retaining only the first-order term of the Bessel function, yielding the following expression:

$$\frac{E_{\text{inc}}}{E_{1}} \simeq J_{0}(m_{\text{a}})J_{0}(m_{\text{b}}) + iJ_{1}(m_{\text{a}})J_{0}(m_{\text{b}})(e^{i\omega_{\text{a}}t} + e^{-i\omega_{\text{a}}t}) + iJ_{0}(m_{\text{a}})J_{1}(m_{\text{b}})(e^{i\omega_{\text{b}}t} + e^{-i\omega_{\text{b}}t})
- J_{1}(m_{\text{a}})J_{1}(m_{\text{b}})(e^{i(\omega_{\text{a}}+\omega_{\text{b}})t} + e^{-i(\omega_{\text{a}}+\omega_{\text{b}})t}) - J_{1}(m_{\text{a}})J_{1}(m_{\text{b}})(e^{i(\omega_{\text{a}}-\omega_{\text{b}})t} + e^{-i(\omega_{\text{a}}-\omega_{\text{b}})t}).$$
(4)

Therefore, light phase-modulated with two modulation frequencies f_a and f_b produces carrier light, the associated PM sidebands, and sum and difference frequency components $(f_a + f_b, f_a - f_b)$.

As stated in Ref. [11], the reflection response of the interferometer can be expressed in matrix form after extending Eq. 4 to include spatial modes. The reflection matrices for the

carrier light and the modulated sidebands (upper: u, lower: l) are distinguished by subscripts as M_c , M_{ua} , M_{la} , M_{ub} , M_{lb} , $M_{u(a+b)}$, $M_{l(a+b)}$, $M_{u(a-b)}$, and $M_{l(a-b)}$. Using these matrices, the reflected light from the interferometer can be expressed as follows:

$$E_{\text{ref}} = \begin{bmatrix} u^{00} & u^{10} \end{bmatrix} \begin{pmatrix} \mathbf{M}_{c} \begin{bmatrix} J_{0}(m_{a})J_{0}(m_{b}) \\ 0 \end{bmatrix} \\ + \mathbf{M}_{\text{ua}} \begin{bmatrix} iJ_{1}(m_{a})J_{0}(m_{b}) \\ 0 \end{bmatrix} e^{i\omega_{a}t} + \mathbf{M}_{\text{la}} \begin{bmatrix} iJ_{1}(m_{a})J_{0}(m_{b}) \\ 0 \end{bmatrix} e^{-i\omega_{a}t} \\ + \mathbf{M}_{\text{ub}} \begin{bmatrix} iJ_{0}(m_{a})J_{1}(m_{b}) \\ 0 \end{bmatrix} e^{i\omega_{b}t} + \mathbf{M}_{\text{lb}} \begin{bmatrix} iJ_{0}(m_{a})J_{1}(m_{b}) \\ 0 \end{bmatrix} e^{-i\omega_{b}t} \\ + \mathbf{M}_{\text{u(a+b)}} \begin{bmatrix} -J_{1}(m_{a})J_{1}(m_{b}) \\ 0 \end{bmatrix} e^{i(\omega_{a}+\omega_{b})t} + \mathbf{M}_{\text{l(a+b)}} \begin{bmatrix} -J_{1}(m_{a})J_{1}(m_{b}) \\ 0 \end{bmatrix} e^{-i(\omega_{a}+\omega_{b})t} \\ + \mathbf{M}_{\text{u(a-b)}} \begin{bmatrix} -J_{1}(m_{a})J_{1}(m_{b}) \\ 0 \end{bmatrix} e^{i(\omega_{a}-\omega_{b})t} + \mathbf{M}_{\text{l(a-b)}} \begin{bmatrix} -J_{1}(m_{a})J_{1}(m_{b}) \\ 0 \end{bmatrix} e^{-i(\omega_{a}-\omega_{b})t} \end{pmatrix} E_{1},$$

$$(5)$$

we assume the optical axis misalignment is small and the reflected light is dominated by the TEM00 and TEM10 modes, so that the electric field amplitude can be expressed using the TEM00 (u^{00}) and TEM10 (u^{10}) [11].

2.3 Derivation of PMPMWFS signals.

The intensity P_{qpd} measured by a QPD can be expressed as follows in terms of the reflected electric field E_{qpd} :

$$P_{\rm qpd} = E_{\rm qpd} E_{\rm qpd}^*. (6)$$

 $E_{\rm qpd}$ represents the electric field at the QPD that detects the interferometer's reflected light, and is calculated by incorporating the light propagation matrix from the interferometer to the QPD into Eq. 5. This propagation matrix is characterized by the distance $l_{\rm pd}$ from the interferometer's reflection point to the QPD and the Gouy phase $\eta_{\rm pd}$ associated with the light propagation between them [11].

$$\begin{split} E_{\rm qpd} &= e^{-ikl_{\rm pd}} \{ E_{\rm c} + E_{\rm ua} e^{i\omega_{\rm a}(t - \frac{l_{\rm pd}}{c})} + E_{\rm la} e^{-i\omega_{\rm a}(t - \frac{l_{\rm pd}}{c})} + E_{\rm ub} e^{i\omega_{\rm b}(t - \frac{l_{\rm pd}}{c})} + E_{\rm lb} e^{-i\omega_{\rm b}(t - \frac{l_{\rm pd}}{c})} \\ &+ E_{\rm u(a+b)} e^{i(\omega_{\rm a}+\omega_{\rm b})(t - \frac{l_{\rm pd}}{c})} + E_{\rm l(a+b)} e^{-i(\omega_{\rm a}+\omega_{\rm b})(t - \frac{l_{\rm pd}}{c})} \\ &+ E_{\rm u(a-b)} e^{i(\omega_{\rm a}-\omega_{\rm b})(t - \frac{l_{\rm pd}}{c})} + E_{\rm l(a-b)} e^{-i(\omega_{\rm a}-\omega_{\rm b})(t - \frac{l_{\rm pd}}{c})} \} E_{1}, \end{split}$$
(7)
$$E_{\rm c} &= \left[\begin{array}{ccc} u^{00} & u^{10} \end{array} \right] \left[\begin{array}{ccc} e^{i\eta_{\rm pd}} & 0 \\ 0 & e^{2i\eta_{\rm pd}} \end{array} \right] M_{\rm c} \left[\begin{array}{ccc} J_{0}(m_{\rm a}) J_{0}(m_{\rm b}) \\ 0 \end{array} \right], \\ E_{\rm xa} &= \left[\begin{array}{ccc} u^{00} & u^{10} \end{array} \right] \left[\begin{array}{ccc} e^{i\eta_{\rm pd}} & 0 \\ 0 & e^{2i\eta_{\rm pd}} \end{array} \right] M_{\rm xa} \left[\begin{array}{ccc} iJ_{0}(m_{\rm b}) J_{1}(m_{\rm a}) \\ 0 \end{array} \right], \\ E_{\rm xb} &= \left[\begin{array}{ccc} u^{00} & u^{10} \end{array} \right] \left[\begin{array}{ccc} e^{i\eta_{\rm pd}} & 0 \\ 0 & e^{2i\eta_{\rm pd}} \end{array} \right] M_{\rm xb} \left[\begin{array}{ccc} iJ_{0}(m_{\rm a}) J_{1}(m_{\rm b}) \\ 0 \end{array} \right], \\ E_{\rm x(a+b)} &= \left[\begin{array}{ccc} u^{00} & u^{10} \end{array} \right] \left[\begin{array}{ccc} e^{i\eta_{\rm pd}} & 0 \\ 0 & e^{2i\eta_{\rm pd}} \end{array} \right] M_{\rm x(a+b)} \left[\begin{array}{cccc} -J_{1}(m_{\rm a}) J_{1}(m_{\rm b}) \\ 0 \end{array} \right], \\ E_{\rm x(a-b)} &= \left[\begin{array}{cccc} u^{00} & u^{10} \end{array} \right] \left[\begin{array}{cccc} e^{i\eta_{\rm pd}} & 0 \\ 0 & e^{2i\eta_{\rm pd}} \end{array} \right] M_{\rm x(a-b)} \left[\begin{array}{ccccc} -J_{1}(m_{\rm a}) J_{1}(m_{\rm b}) \\ 0 \end{array} \right], \\ x &= (\mathrm{u}, \mathrm{l}). \end{split}$$

To demodulate $P_{\rm qpd}$ at two sideband difference frequencies, the angular frequency $\omega_{\rm a} - \omega_{\rm b}$ components in $P_{\rm qpd}$ are summarized as follows:

$$\frac{\{P_{\rm qpd}\}_{\omega_{\rm a}-\omega_{\rm b}}}{|E_1|^2} = 2Re\{(E_{\rm c}E_{\rm l(a-b)}^* + E_{\rm c}^*E_{\rm u(a-b)} + E_{\rm ua}E_{\rm ub}^* + E_{\rm la}^*E_{\rm lb})e^{i(\omega_{\rm a}-\omega_{\rm b})(t-\frac{l_{\rm pd}}{c})}\}.$$
 (8)

When the horizontal, vertical, and light propagation directions are taken as the x-, y-, and z-directions, respectively, the amplitude distributions of u^{00} and u^{10} on the x-z plane are expanded under the assumption tilting along the x-axis [12]:

$$u^{00}(x,z) = \left(\frac{2}{\pi\omega^2(z)}\right)^{\frac{1}{4}} \exp\left[-\left(\frac{x}{\omega(z)}\right)^2 - i\frac{kx^2}{2R(z)}\right],\tag{9}$$

$$u^{10}(x,z) = \left(\frac{2}{\pi\omega^{2}(z)}\right)^{\frac{1}{4}} \frac{2x}{\omega(z)} \exp\left[-\left(\frac{x}{\omega(z)}\right)^{2} - i\frac{kx^{2}}{2R(z)}\right],\tag{10}$$

where the curvature radius of the beam wavefront is denoted by R(z), and the beam radius at position z is denoted by $\omega(z)$. Since $u^{00}(x,z)$ is an even function in Eq. 9 and $u^{10}(x,z)$

is an odd function in Eq. 10. Consequently, the terms $|u^{00}|^2$ and $|u^{10}|^2$ are both even, while the terms $u^{00}u^{10*}$ and $u^{10}u^{00*}$ are odd. The WFS signal is obtained by taking the difference between the positive and negative regions along the x-axis using a photo diode divided into two halves along the x-axis like a QPD. Consequently, the terms $|u^{00}|^2$ and $|u^{10}|^2$ are canceled out, while only the cross terms $u^{00}u^{10*}$ and $u^{10}u^{00*}$ in Eq. 8 contribute to the signal.

$$2\int_0^\infty u^{00}(x,z)u^{10*}(x,z)dx = 2\int_0^\infty u^{00*}(x,z)u^{10}(x,z)dx = \sqrt{\frac{2}{\pi}}.$$
 (11)

Given that Eq. 11 and $J_0(m_a)J_0(m_b)J_1(m_a)J_1(m_b)$ are real-valued, the following expression can be obtained:

$$\frac{P_{\text{PMPMWFS}}}{2\sqrt{\frac{2}{\pi}}J_{0}(m_{\text{a}})J_{0}(m_{\text{b}})J_{1}(m_{\text{a}})J_{1}(m_{\text{b}})}
= Re\left[\left\{\left(-M_{\text{c}}^{00*}M_{\text{u(a-b)}}^{10} - M_{\text{c}}^{10}M_{\text{l(a-b)}}^{00*} + M_{\text{ua}}^{10}M_{\text{ub}}^{00*} + M_{\text{la}}^{00*}M_{\text{lb}}^{10}\right)e^{i\eta_{\text{pd}}}
+ \left(-M_{\text{c}}^{00}M_{\text{l(a-b)}}^{10*} - M_{\text{c}}^{10*}M_{\text{u(a-b)}}^{00} + M_{\text{ua}}^{00}M_{\text{ub}}^{10*} + M_{\text{la}}^{10*}M_{\text{lb}}^{00}\right)e^{-i\eta_{\text{pd}}}\right\}e^{i(\omega_{\text{a}}-\omega_{\text{b}})(t-\frac{l_{\text{pd}}}{c})}\right].$$
(12)

We distinguish the 00 and 10 components of the reflection matrix M for the composite optical resonator by superscripts such as M^{00} and M^{10} . Furthermore, under the condition that the misalignment is sufficiently small, M^{10} can be expressed linearly with respect to the angle of each mirror [11]. A conventional WFS detects the misalignment signal between the carrier and the PM sideband. From Eq. 12, it is evident that the PMPMWFS signal detects the relative misalignment between the sideband f_a and f_b , as well as between the carrier and the difference frequency $f_a - f_b$. It was also demonstrated that the PMPMWFS signal varies due to the Gouy phase from the interferometer reflection to a QPD.

3 PMPMWFS signal in the PRXARM of KAGRA.

To verify the response of the PMPMWFS signal, we performed theoretical calculations and experimental measurements using the PRXARM at KAGRA. The detailed configuration of the PRXARM employed in this Sec. 3 is outlined in Sec. 3.1. In Section 3.2, we derive the PMPMWFS signals for angular variations of each mirror in the PRXARM configuration presented in Sec. 3.1, and compare with the conventional WFS signal using the carrier and PM sideband beat signal. In Section 3.3, we experimentally measure the signals in KAGRA's PRXARM. In Section 3.4, we demonstrate feedback control using the PMPMWFS signal on KAGRA's PRXARM.

3.1 PRXARM of KAGRA

The PRXARM in KAGRA is an optical resonator consisting of the X-arm cavity and PRC (Fig. 2). The mirrors constituting the PRXARM are summarized below. The X-arm cavity consists of Input Test Mass X (ITMX) and End Test Mass X (ETMX) mirrors. PRC comprises PRM, Power Recycling mirror 2(PR2), 3(PR3) and ITMX. PR2 and PR3 are placed to adjust the Gouy phase between PRM and ITMX. Input Mode-Matching Telescope 1 and 2 (IMMT1 and IMMT2) are mirrors used to adjust the incident optical axis into PRC. For the PRXARM measurement, to avoid interference from the Y-arm cavity, ITMY was misaligned.

The incident light power was 1 W. The incident light was phase-modulated with an eighth harmonic ($f_2 = 45.02 \text{ MHz}$) and an tenth harmonic ($f_3 = 56.27 \text{ MHz}$) of the seed frequency ($f_{\text{seed}} = 5.63 \text{ MHz}$). When the carrier resonates in the entire PRXARM, f_2 resonates in PRC and anti-resonates with the X-arm cavity, while f_3 anti-resonates with the entire composite optical resonator.

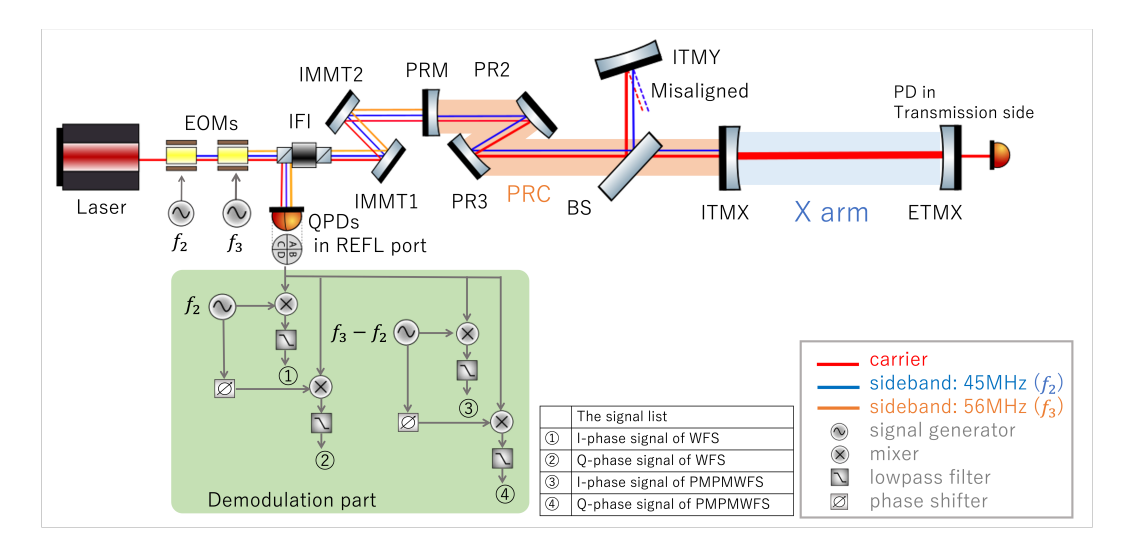


Fig. 2: Schematic of the PRXARM configuration in KAGRA. Red, blue, and orange lines indicate the optical paths for the carrier, f_2 sideband, and f_3 sideband, respectively. The WFS and PMPMWFS signals are obtained by demodulating the QPD signals on the REFL port at frequencies f_2 and $f_3 - f_2$, respectively, and then passing them through low-pass filters. The demodulated WFS signal is separated into the I-phase signal (at the reference demodulation phase) and the Q-phase signal (phase-shifted by 90 degrees from the reference). The X-arm cavity transmission power is detected by a photodiode at its transmission port.

3.2 Theoretical calculations for the PRXARM.

This section discusses the PMPMWFS signal obtained in the PRXARM.

We derive the reflected signal response when the PRM, PR2, PR3, ITMX, and ETMX mirrors are each tilted by 0.1 nrad, in order to calculate the I-phase and Q-phase signals of the WFS signal using Eq. 12 in PRXARM. The signal responses are shown in Tab. 1, 2 and 3.

mirror	$M_{ m c}^{10}$	$M_{\mathrm{u}(f_2)}^{10}$	$M_{\mathrm{l}(f_2)}^{10}$
PR3	$-5.6 \times 10^2 + 4.5 \times 10^2 i$	$-6.3 \times 10^4 - 1.1 \times 10^4 i$	$-1.9 \times 10^4 + 6.2 \times 10^4 i$
PR2	$-1.4 \times 10^2 + 23i$	$-7.7 \times 10^3 - 1.3 \times 10^3 i$	$-2.3 \times 10^3 + 7.5 \times 10^3 i$
PRM	$7.9 \times 10^3 - 2.3 \times 10^4 i$	$-2.4 \times 10^4 + 1.2 \times 10^4 i$	$8.3 \times 10^3 + 2.5 \times 10^4 i$
ITMX	$-8.6 \times 10^3 - 4.4 \times 10^3 i$	$3.0 \times 10^4 + 5.2 \times 10^3 i$	$9.1 \times 10^3 - 3.0 \times 10^4 i$
ETMX	$1.5 \times 10^4 + 6.9 \times 10^3 i$	$-2.4 \times 10^2 - 42i$	$56 - 1.8 \times 10^2 i$

Table 1: Each element of reflection matrices for the carrier and f_2 . Each value represents the Matrix element normalized by the inclination of each mirror.

mirror	$M_{{ m u}(f_3)}^{10}$	$M_{\mathrm{l}(f_3)}^{10}$
PR3	$-3.5 \times 10^4 - 4.2 \times 10^4 i$	$2.3 \times 10^4 + 1.8 \times 10^4 i$
PR2	$-4.2 \times 10^3 - 5.1 \times 10^3 i$	$2.9 \times 10^3 + 2.2 \times 10^3 i$
PRM	$9.5 \times 10^3 - 2.3 \times 10^4 i$	$5.7 \times 10^3 - 2.4 \times 10^4 i$
ITMX	$1.7 \times 10^4 + 2.0 \times 10^4 i$	$-1.1 \times 10^4 - 8.8 \times 10^3 i$
ETMX	31 + 37i	57 + 44i

Table 2: Each element of reflection matrices for f_3 . Each value represents the Matrix element normalized by the inclination of each mirror.

As described in Sec. 2.3, the PMPMWFS signal comprises the component arising from the beat signal between the f_2 and f_3 sidebands, as well as from the beat between the carrier and the difference frequency. Consequently, the results are presented together. The conventional WFS signal [7] was demodulated at the REFL port using f_2 . To compare it with the PMPMWFS calculation results, it was calculated under identical conditions as in

mirror	$M_{\mathrm{u}(f_3-f_2)}^{10}$	$M_{{ m l}(f_3-f_2)}^{10}$
PR3	$-4.8 \times 10^3 - 9.8 \times 10^3 i$	$1.3 \times 10^4 - 2.6 \times 10^3 i$
PR2	$-5.8 \times 10^2 - 1.2 \times 10^3 i$	$1.6 \times 10^3 - 3.2 \times 10^2 i$
PRM	$7.0 \times 10^3 + 2.5 \times 10^4 i$	$-2.1 \times 10^4 + 1.5 \times 10^4 i$
ITMX	$2.3 \times 10^3 + 4.7 \times 10^3 i$	$-6.3 \times 10^3 + 1.3 \times 10^3 i$
ETMX	3.4 + 6.9i	46 - 9.3i

Table 3: Each element of reflection matrices for $f_3 - f_2$. Each value represents the Matrix element normalized by the inclination of each mirror.

Sec. 2 using the following equation:

$$\begin{split} &\frac{P_{\text{WFS}}}{2\sqrt{\frac{2}{\pi}}J_0(m_{\text{a}})J_0^2(m_{\text{b}})J_1(m_{\text{a}})}\\ &=Re[i\{(-M_{\text{c}}^{10}M_{\text{la}}^{00*}+M_{\text{c}}^{00*}M_{\text{ua}}^{10})e^{i\eta_{\text{pd}}}+(-M_{\text{c}}^{00}M_{\text{la}}^{10*}+M_{\text{c}}^{10*}M_{\text{ua}}^{00})e^{-i\eta_{\text{pd}}}\}e^{i\omega_{\text{a}}(t-\frac{l_{\text{pd}}}{c})}]. \end{split}$$

At first, we plotted the result in polar coordinates on the I-Q plane, with the demodulation phase adjusted to minimize the ETMX angle signal in the I-phase component (Fig. 3). Note that the Gouy phase was set to 0 degrees in these calculations.

Figure 4 shows the Gouy phase dependence of the magnitude of the I-phase and Q-phase signals. The calculation in Fig. 4 was performed using the demodulation phase determined in Fig. 3. The results reveal the following.

- The amplitude of the PMPMWFS signal is generally less than one-tenth compared to the WFS signal. This is because WFS uses the beat between the one PM sideband and the carrier, whereas PMPMWFS is demodulated based on the beat component between the two PM sidebands. In this calculation, the modulation indices for sideband 2 and sideband 3 are set to 0.15. As a result, the amplitude is reduced due to differences in the coefficients of the Bessel functions.
- The ETMX angle signal is scarcely visible in the beat signal between f_2 and f_3 . This is likely because that both f_2 and f_3 are anti-resonant with the X-arm cavity, making them insensitive to the misalignment of the X-arm cavity's optical axis.
- By choosing an appropriate Gouy phase, the PRM angle signal can be detected with higher sensitivity than those of the other mirrors.
- The optimal demodulation phase for the ETMX angle signal and the other mirrors is close to 90 degrees in the PMPMWFS signal. Conversely, in the conventional WFS signal, the phase difference between each mirror angle signal is close to 0 degrees

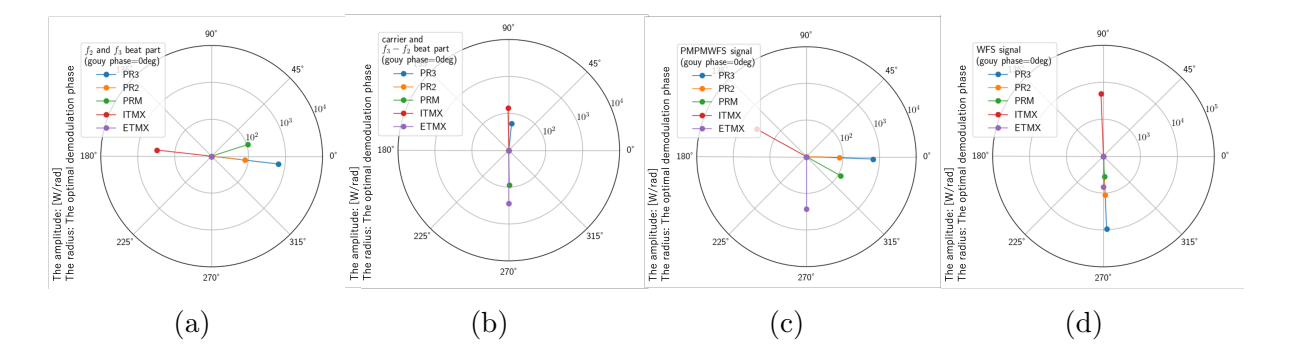


Fig. 3: I-Q plane plot calculated for the PMPMWFS signal and conventional WFS signal in PRXARM. The radial axis is plotted on a logarithmic scale. Figure 3a shows the beat component between the f_2 and f_3 sidebands. Figure 3b shows the beat component between the carrier and the difference frequency $(f_3 - f_2)$ sideband, and Fig. 3c shows the PMPMWFS signal obtained by combining these components, while Fig. 3d shows the calculated WFS signal. The argument represents the optimal demodulation phase in degrees at which the signal from each mirror is maximized. The magnitude represents the signal normalized by the tilt of each mirror. Note that the Gouy phase was calculated assuming 0 degrees. Furthermore, the demodulation phase for all degrees of freedom was rotated so that the ETMX angle signal in the I-phase component was minimized for both PMPMWFS and conventional WFS results. The rotated phase applied in Fig. 3c was also applied in Fig. 3a and 3b.

or 180 degrees. Consequently, the PMPMWFS signal enables efficient decoupling of the ETMX angle signal from the others.

3.3 Comparison between the measurement and the theoretical calculation in the PRXARM

An optical system was constructed using KAGRA's PRXARM to acquire both the PMPMWFS and the conventional WFS signals. In particular, QPDs were positioned to achieve the Gouy phases of -55 degrees and 50 degrees, respectively, in order to separate the degrees of freedom for translational and tilt misalignments along the relative optical axis. Each mirror was oscillated at a frequency of 1.3 Hz, separately in the pitch and yaw directions. The PMPMWFS and WFS signals were measured and normalized by the tilt of each mirror, which was monitored using the optical lever.

The results, plotted on the I-Q plane based on measurements taken with each mirror tilted in the pitch angle, are shown in Figure 5a and 5b. To compare with the calculations, the I-Q plane plots of the PMPMWFS and WFS signals calculated at the Gouy phases of -55 degrees and 50 degrees are shown in Fig. 5c and 5d, respectively. Note that the demodulation

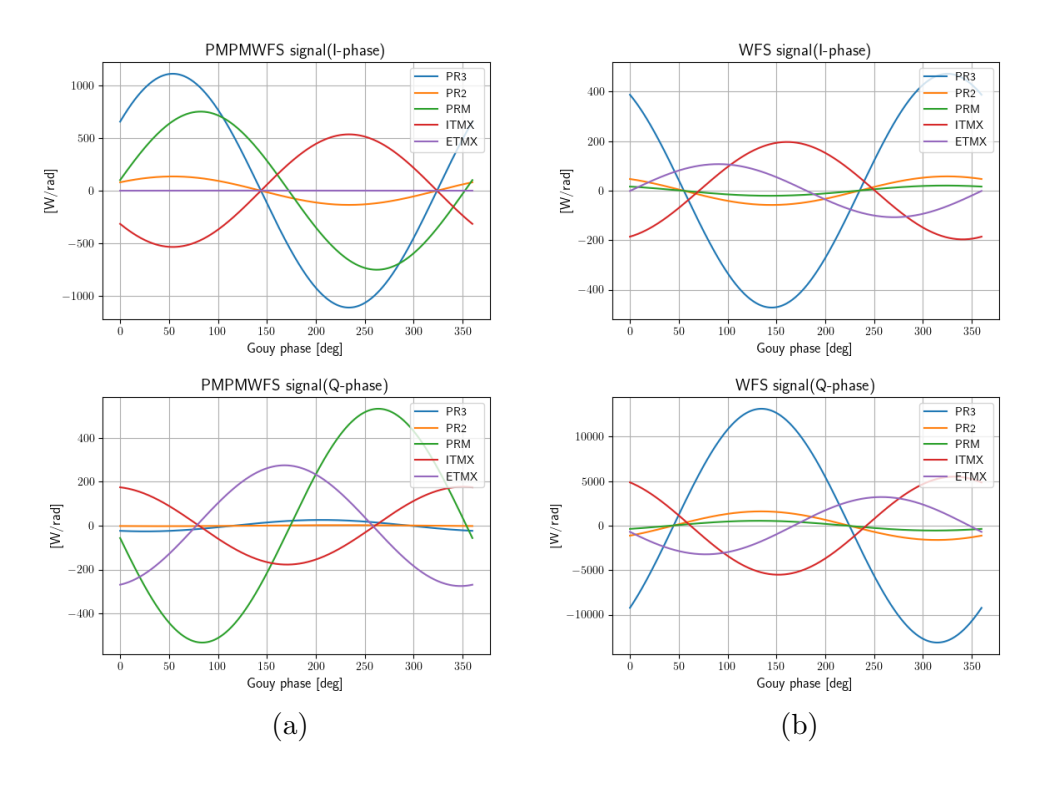


Fig. 4: Gouy phase dependence of the magnitude of I-phase and Q-phase signals when the Gouy phase $\eta_{\rm pd}$ is swept from -180 to 180 degrees. The horizontal axis represents the Gouy phase $\eta_{\rm pd}$ degrees, and the vertical axis represents the signal magnitude normalized by the mirror angle angle. The Figures 4a and 4b show the graphs of the PMPMWFS and WFS signals, respectively. The upper and lower figures show the graphs of I-phase and Q-phase signals, respectively. The demodulation phase is set such that the ETMX angle signal is minimized in the I-phase at the Gouy phase of 0 degrees.

phase here is rotated such that the ETMX angle signal reached its minimum at I-phase. From these graphs, the following can be observed:

- As predicted by theoretical calculations, the amplitude of the PMPMWFS signal is consistently less than one-tenth of that of the conventional WFS signal.
- It is either in phase or opposite phase with all degree of freedom in the conventional WFS signals, whereas the optimal demodulation phase for the PRM and ETMX angle signals in the PMPMWFS signals is orthogonal to that of the other angle signals.
- Comparison of the experimental and theoretical results for the PMPMWFS signal, the optimal demodulation phase of the PRM angle signal is different. This difference

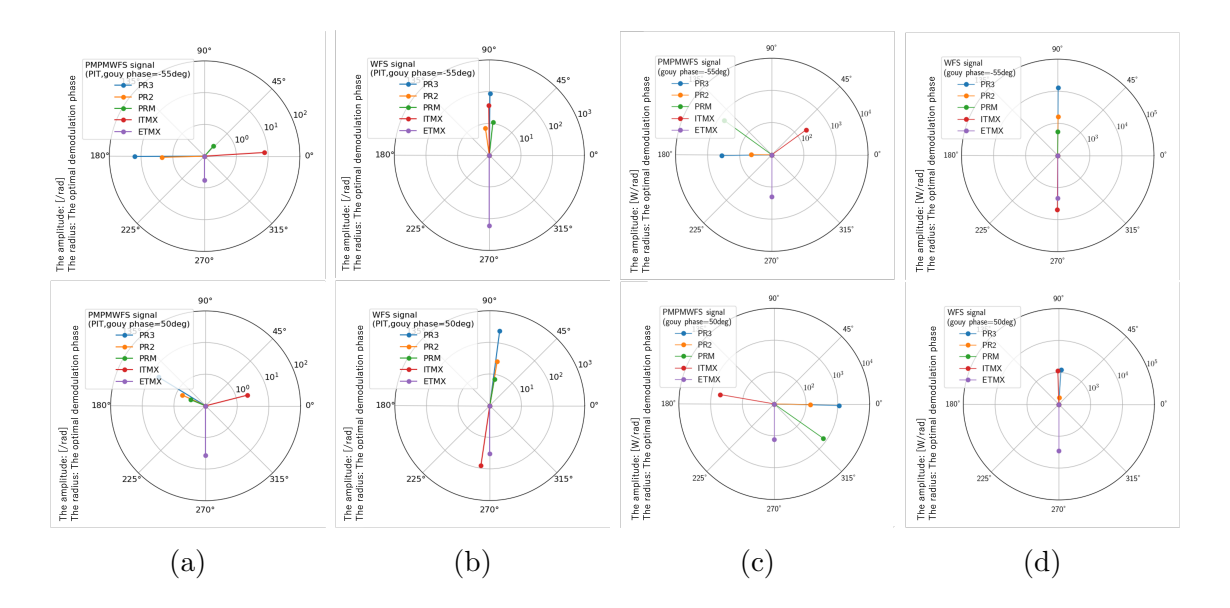


Fig. 5: Measured results and theoretical calculation results for the PRXARM. Figure 5a and 5b show the PMPMWFS and WFS signals obtained by tilting each mirror in the pitch angle. The signals in Fig. 5a and 5b were obtained by normalizing the measured values to the local tilt of each mirror measured by the optical lever, when each mirror was periodically tilted at 1.3 Hz. Figure 5c and 5d present the corresponding theoretical results. The upper row of each plot corresponds to the Gouy phase of -55 degrees, while the lower row corresponds to the Gouy phase of 50 degrees. Each plot shows the signals with the demodulation phase rotated to minimize the ETMX angle signal in the I-phase component.

- may be caused by the larger misalignment from the optimal position during the experiment, although the exact cause remains unclear.
- The results for some degrees of freedom exhibit sign flips. In particular, the PMPMWFS results at a Gouy phase of 50 degrees in Fig. 5a show a sign flip in all degrees of freedom except for the ETMX angle signal, whereas the WFS results at a Gouy phase of 50 degrees in Fig. 5b show a sign flip only for the ITMX angle signal. These sign flips can be explained by the Gouy phases of 79 degrees and 63 degrees in the PMPMWFS and WFS calculations, respectively. However, it is unlikely that the Gouy phase at the QPD location differs by more than 12 degrees, considering the beam waist position and Rayleigh range estimated from the measured beam profile. The cause of these discrepancies remains unclear.

Based on the above results, the PMPMWFS has an advantage in decoupling the arm-axis fluctuation from the others compared with the conventional WFS. However, it should be noted that the signal amplitude is reduced due to the Bessel-function terms.

Measurements in the yaw angle were also shown in Fig. 6. The results similarly showed that the PMPMWFS signal detects ETMX orthogonally. The Section 3.4 examines whether control can actually be implemented based on these results.

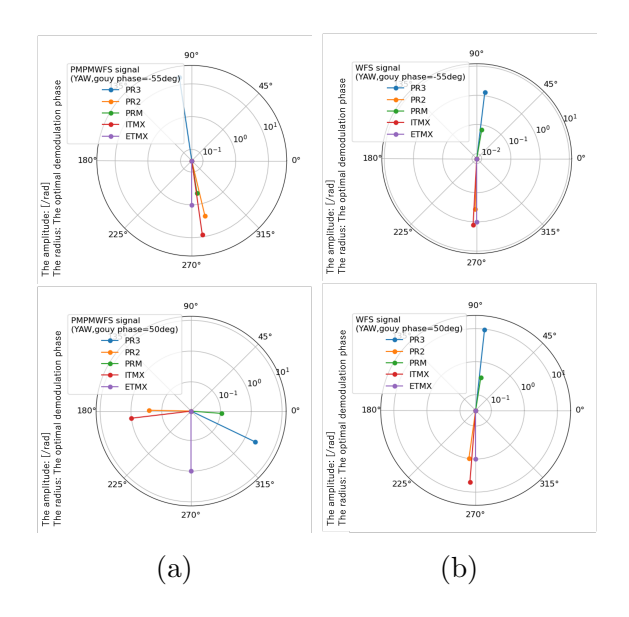


Fig. 6: Measurement results for the PRXARM. Figure 6a and 6b show the PMPMWFS and WFS signals obtained by tilting each mirror in the yaw angle, respectively. The signals in Fig. 5a and 5b were obtained by normalizing the angular motions of each mirror measured by the optical lever, when each mirror was periodically tilted at 1.3 Hz. The upper row of each plot corresponds to the Gouy phase of -55 degrees, while the lower row corresponds to the Gouy phase of 50 degrees. Each plot shows the signals with the demodulation phase rotated to minimize the ETMX angle signal in the I-phase component.

3.4 Demonstration of alignment control with PMPMWFS signals

To verify the controllability of the optical axis using the PMPMWFS signal, the alignment sensing and control using PMPMWFS was implemented in KAGRA's PRXARM, based on the results presented in Sec. 3.3.

Figure 5c and 5d show that the pitch and yaw angle signals of PR3 were significantly detected by the QPD1 signal at the Gouy phase of -55 degrees. Therefore, the PMPMWFS signal detected by the QPD1 signal was used as the PR3 control. Furthermore, since the optical axis in the PRXARM consists of three axes, namely the X-arm cavity, the PRC, and the incident-light axis, three mirrors were necessary to correct the overall relative misalignment. Consequently, the Alignment Dither System (ADS) [13] was implemented for the mirrors that were not controlled by the PMPMWFS feedback signal. The demodulation phase of the QPD1 signal was adjusted so that the magnitude of the PR3 pitch signal was maximized in the I-phase signal, and the demodulation phase of the signals of the QPD at Gouy phase of 50 degrees (QPD2) was adjusted so that the ETMX I-phase signal was minimized. Furthermore, the ETMX and PRM angle signals were decoupled by appropriately combining two QPD signals. Consequently, the pitch signal $(S_{\rm pitch})$ and yaw signal $(S_{\rm yaw})$ for PMPMWFS, obtained from the I-phase signal $(S_{\rm X})$ and Q-phase signal $(S_{\rm X})$ from QPDX, are expressed as follows.

$$S_{\text{pitch}} = 2.232S_1^{\text{I}} + 1.000S_2^{\text{Q}} \tag{13}$$

$$S_{\text{yaw}} = 2.599S_1^{\text{I}} - 9.522S_2^{\text{I}} + 1.000S_2^{\text{Q}}$$
(14)

At this time, S_{pitch} and S_{yaw} obtained when each mirror was tilted by 1 µrad are summarized in Tab. 4. The signal amplitudes of the ETMX and PRM angle signal are less than one-tenth of those of the PR3 angle signal, indicating that the signals are well decoupled.

[Count/urad]	ITMX	ETMX	PRM	PR2	PR3
Error signal of pitch	22.77	3.988	0.3700	5.837	53.59
Error signal of yaw	74.73	4.554	3.730	20.72	136.2

Table 4: S_{pitch} and S_{yaw} values when each mirror was tilted by 1 urad.

Pitch and yaw of PR3 were controlled by S_{pitch} and S_{yaw} . Figure 7 shows the Open Loop Transfer Functions (OLTFs) of the pitch and yaw controls. The Unity Gain Frequencies (UGFs) for pitch and yaw were 0.4 Hz and 0.6 Hz, respectively, and the phase margin at the UGFs was 60 degrees and 50 degrees, respectively, indicating robust control performance.

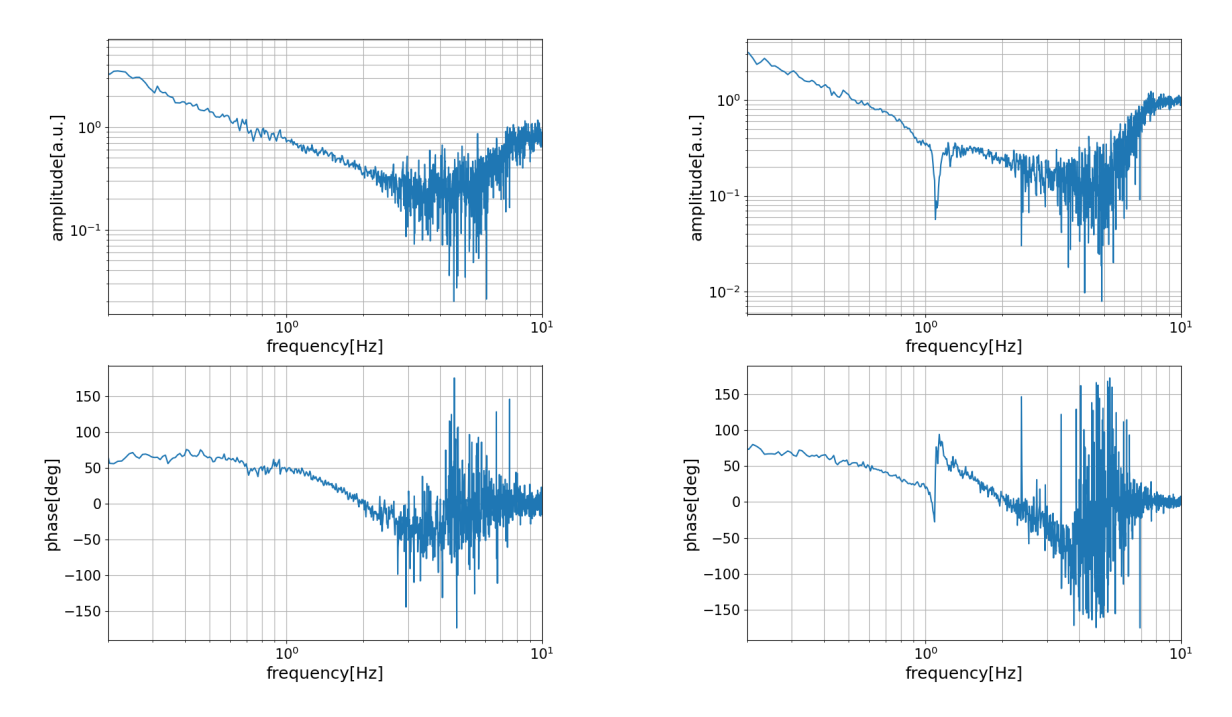


Fig. 7: OLTF of PR3 control with S_{pitch} and S_{yaw} . The left figure is OLTF of the pitch control. The right figure is OLTF of the yaw control. Since the signal-to-noise ratio of data exceeding 2 Hz has low signal-to-noise ratio, the data only up to 10 Hz are shown.

With the WFS control enabled, the interferometer kept locking stably for more than 1 hour as shown in Fig. 8. When the control was turned on, the transmission power increased. This observation confirms that the ASC using PMPMWFS is effective for interferometer alignment sensing and control.

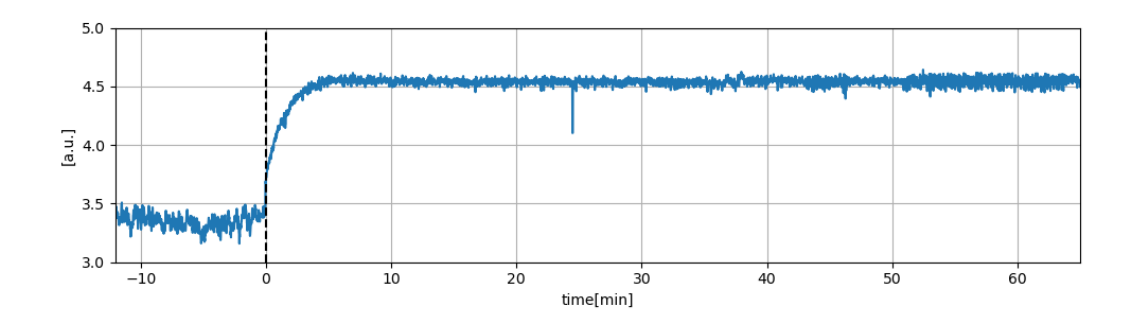


Fig. 8: Transmission power of the X-arm cavity, normalized by the transmission power when the X-arm cavity is resonating with misaligned PRM. The black dotted line indicates when all ASC turned on.

4 Conclusion.

To decouple signals from the arm cavity axis misalignment to the other optical axis misalignments, we propose a new WFS technique (PMPMWFS) that demodulates the difference frequency using two sidebands that do not resonate in the arm cavities. We derived the theoretical equations and compared them with the experiments using the PRXARM in KAGRA. The PMPMWFS signal measures the relative misalignment between the carrier and the difference frequency $f_a - f_b$, and the relative misalignment between two sidebands, thereby demonstrating a signal response that is distinct from that of the WFS signal. Furthermore, in the PRXARM, signal separation was achieved because the ETMX angle signals appeared orthogonally. Finally, we demonstrated alignment control using the PMPMWFS signal, thereby validating this technique as a viable detection signal.

Acknowledgment

This work was supported by JST SPRING, Grant Number JPMJSP2121, Ministry of Education, Culture, Sports, Science and Technology (MEXT), Japan Society for the Promotion of Science (JSPS) in Japan; National Research Foundation (NRF) and Ministry of Science and ICT (MSIT) in Korea; Academia Sinica (AS) and National Science and Technology Council (NSTC) in Taiwan.

Appendix.Parameters used in the PRXARM calculation

The parameters used in the calculations for Sec. 3.2 and Sec. 3.3 are summarised in Tab. 5.

	power [W] wavele	ength [nm]		
laser	1.0	064.0		
EOM	frequency [MHz]	modulati	on index modulati	on type
	$f_{\rm seed} = 5.627$			
EOM2	$f_{\rm seed}*8.0$	0.1	phase mo	dulation
EOM3	$f_{\rm seed}*10.0$	0.1	phase mo	dulation
space		length [m]	gouy phase [deg]	
from I	MMT1 to IMMT2	3.105	1.965	
from I	MMT2 to PRM	4.8416	4.519	
from P	RM to PR2	14.7615	14.124	
from P	R2 to PR3	11.0661	1.278	
from P	R3 to BS	15.7638	0.225	
from E	S to ITMX	26.6649	0.391	
from I'	ΓMX to ETMX	3.000e3	126.078	
mirror	Transmittance	Loss	curvature radius [m]	incident angle [deg]
IMMT	1 0.0078	0.00	-8.91	3.6
IMMT	2 0.0078	0.00	14.005	3.6
PRM	0.10	45.0e-6	-458.1285	
PR2	500.0e-6	45.0e-6	-3.0764	0.6860
PR3	50.0e-6	45.0e-6	-24.9165	0.6860
BS	0.50	0.00	∞	45.0
ITMX	0.0040	45.0e-6	-1900.0	
ETMX	5.0e-06	45.0e-6	1900.0	

Table 5: Parameters used in the theoretical calculations. The radius of curvature of each mirror is defined with respect to its non-black surface, as shown in Fig. 2. For ITMX, the mirror thickness (0.15 m) and the refractive index of the substrate ($n_{\rm ITMX} = 1.754$) were also taken into account in the calculations.

References

- [1] A. Einstein, "Die Grundlage der allgemeinen Relativitätstheorie," Annalen der Physik, vol. 354, no. 7, pp. 769-822, 1916, 10.1002/andp.19163540702
- [2] M. Soares-Santos et al. (The LIGO Scientific Collaboration and the Virgo Collaboration), "First measurement of the Hubble constant from a dark standard siren using the Dark Energy Survey galaxies and the LIGO/Virgo binary-black-hole merger GW170814," The Astrophysical Journal Letters, vol. 876, no. 1, p. L7, Apr. 2019, 10.3847/2041-8213/ab14f1
- [3] R. Abbott et al. (LIGO Scientific Collaboration and Virgo Collaboration), "Tests of general relativity with binary black holes from the second LIGO-Virgo gravitational-wave transient catalog," *Phys. Rev. D*, vol. 103, no. 12, p. 122002, Jun. 2021, 10.1103/PhysRevD.103.122002
- [4] J. Aasi et al. (The LIGO Scientific Collaboration), "Advanced LIGO," Classical and Quantum Gravity, vol. 32, no. 7, p. 074001, Mar. 2015, 10.1088/0264-9381/32/7/074001
- [5] F. Acernese et al., "Advanced Virgo: A second-generation interferometric gravitational wave detector," Class. Quantum Grav., vol. 32, no. 2, p. 024001, Dec. 2014, 10.1088/0264-9381/32/2/024001
- [6] B. P. Abbott et al. (LIGO Scientific Collaboration and Virgo Collaboration), "GW170814: A three-detector observation of gravitational waves from a binary black hole coalescence," *Phys. Rev. Lett.*, vol. 119, no. 14, p. 141101, Oct. 2017, 10.1103/PhysRevLett.119.141101
- [7] E. Morrison et al., "Automatic alignment of optical interferometers," Appl. Opt., vol. 33, no. 22, pp. 5041-5049, Aug. 1994, 10.1364/AO.33.005041
- [8] T. Akutsu et al. (for the KAGRA Collaboration), "Overview of KAGRA: Detector design and construction history," Progress of Theoretical and Experimental Physics, vol. 2021, no. 5, p. 05A101, May 2021, 10.1093/ptep/ptaa125
- [9] T. Ushiba (for the KAGRA Collaboration), "Status of the underground gravitational wave detector KAGRA," PoS, vol. TAUP2023, p. 116, 2024, 10.22323/1.441.0116
- [10] J. Mizuno et al., "Resonant sideband extraction: a new configuration for interferometric gravitational wave detectors," Phys. Lett. A, vol. 175, no. 5, pp. 273-276, 1993, 10.1016/0375-9601(93)90620-F
- [11] Y. Hefetz et al., "Principles of calculating alignment signals in complex resonant optical interferometers," J. Opt. Soc. Am. B, vol. 14, no. 7, pp. 1597-1606, Jul. 1997, 10.1364/JOSAB.14.001597
- [12] A. E. Siegman, Lasers, 1st ed. Mill Valley, CA, USA: University Science Books, 1986, http://www.amazon.com/exec/obidos/redirect?tag=citeulike07-20&path=ASIN/0935702113
- [13] K. Kawabe et al., "Automatic alignment-control system for a suspended Fabry-Perot cavity," Appl. Opt., vol. 33, no. 24, pp. 5498-5505, Aug. 1994, 10.1364/AO.33.005498